Single step synthesis of W-modified $LiNiO_2$ using an ammonium tungstate flux†

Damian Goonetilleke, [a] Andrey Mazilkin, [abc] Daniel Weber, [a] Yuan Ma, [a] François Fauth, [d] Jürgen Janek, [ae] Torsten Brezesinski [a] and Matteo Bianchini ‡*[af]

$LiNiO_2$ has long been considered a promising cathode material owing to its high energy density. However, structural and surface instabilities, coupled with its complex synthesis, have thus far prevented its commercialisation. To address these issues, we demonstrate here the use of an ammonium tungstate flux to modify both the crystal structure and primary particle morphology of $LiNiO_2$. Successful synthesis was confirmed using a combination of electron microscopy and synchrotron-based X-ray diffraction (XRD). Refinement of structural models against the data suggests that tungsten dopant ions occupy the Ni site and concurrently induce migration of Ni^{2+} to Li sites. Variable temperature XRD was used to demonstrate the improved stability of the W-doped materials during calcination at high temperatures. Electrochemical characterisation shows that W-modified $LiNiO_2$ offers improved cycle life at the expense of little specific capacity. The structural consequences of tungsten doping on the behaviour of the material during electrochemical cycling were also investigated using *operando* XRD, showing reduced mechanical stress upon cycling. In conclusion, the hereby-reported $LiNiO_2$ modified with W *via* a simple route and no additional processing steps exhibits improved chemomechanics, longer cycling life and structural stability at high temperatures, offering a path towards the reliable synthesis of $LiNiO_2$ with controlled morphology.

Introduction

Lithium-ion batteries (LIBs) are used in a variety of different electrochemical devices at different scales and capacities, from wearable medical devices to portable electronics and power tools, and more recently electric cars and stationary energy storage applications.[1–4] In each of these, the composition, structure, microstructure and morphology of the anode and cathode materials have been carefully optimised to create the best compromise between the energy density (specific or volumetric), rate capability, lifetime and cost for the desired application.[5–9] Recently, the demand for higher energy densities, coupled with a desire to reduce the demand for Co, has promoted the investigation of Ni-rich materials such as nickel cobalt manganese (NCM) and nickel cobalt aluminium (NCA) oxides, with compositions approaching the lithium nickel oxide ($LiNiO_2$, LNO) end-member.[10–15] LNO was identified as a cathode active material (CAM) in the early 1990s,[16–18] however issues with the complexity of its synthesis, and observations of structural and surface instabilities during cycling and handling of the material prevented its widespread adoption.[19–21]

In tandem with the development of new compositions, advanced processing techniques have also been used to optimise the particle morphology and surface features of cathode materials.[22,23] Controlling the morphology of cathode materials is a common subject in industry but has not received as much attention in academia.[24,25] The morphology of Ni-rich layered materials is largely inherited from hydroxide precursor materials.[26,27] Thus, commercially produced Ni-rich cathode materials typically adopt a morphology consisting of spherical secondary particles, which are themselves composed of smaller primary particles with typical average diameters of 10 μm and 100 nm, respectively. This morphology presents a high surface area-to-volume ratio, beneficial for electrochemical (de-)intercalation, but which can promote side reactions with carbonate-based electrolytes. Moreover, mechanical stresses at grain

[a]*Battery and Electrochemistry Laboratory, Institute of Nanotechnology, Karlsruhe Institute of Technology (KIT), Hermann von Helmholtz Platz 1, 76344 Eggenstein Leopoldshafen, Germany. E mail: matteo.bianchini@uni bayreuth.de*

[b]*Institute of Nanotechnology, Karlsruhe Institute of Technology (KIT), Hermann von Helmholtz Platz 1, 76344 Eggenstein Leopoldshafen, Germany*

[c]*Institute of Solid State Physics, Russian Academy of Sciences, Ac. Ossipyan Str. 2, 142432 Chernogolovka, Russia*

[d]*CELLS ALBA Synchrotron, E 08290 Cerdanyola del Vallès, Barcelona, Spain*

[e]*Institute of Physical Chemistry, Center for Materials Research (ZfM/LaMa), Justus Liebig University Giessen, Heinrich Buff Ring 17, 35392 Giessen, Germany*

[f]*BASF SE, Carl Bosch Strasse 38, 67056 Ludwigshafen, Germany*

† Electronic supplementary information (ESI) available. See DOI: 10.1039/d1ta10568j

‡ Current affiliation: University of Bayreuth and Bavarian Center for Battery Technology (BayBatt), Universitatsstraße 30, 95447 Bayreuth, Germany.

boundaries between primary particles, due to anisometric expansion and contraction during (de-)lithiation, can favour inter-granular fracture, exposing new surfaces and increasing cell resistance, which reduces the cell lifetime.[28 30]

Recent reports have shown that the cycle life of these materials can be improved significantly by preparing "single crystals", or rather "monolithic" particles, which effectively suppress the onset of intra-granular fracture during cycling by eliminating the presence of grain boundaries between primary particles.[31 33] Achieving this morphology generally requires non-spherical precursor materials, and/or high synthesis temperatures to promote particle growth.[34] Some authors have also achieved this morphology in Ni-rich compositions, beginning from spherical precursor materials, by using a multi-step annealing process.[35 38] However, this has yet to be reported for the LNO end-member composition, because its structure is quite sensitive to synthesis conditions. The parameters which favour particle growth, higher temperatures and longer annealing times can result in the formation of LNO with higher off-stoichiometry between the Li and Ni sites ($Li_{1-z}Ni_{1+z}O_2$), which leads to poor electrochemical performance.[39,40] At the lower synthesis temperatures conventionally used for materials with high Ni contents (typically θ < 800 °C for Ni > 90%), the opportunity for primary particle growth is somewhat limited. Hence, other methods should be pursued to promote the growth of larger primary particles, as this would still reduce the surface area-to-volume ratio and the quantity of grain boundaries, which may be ultimately favourable for obtaining slower degradation and longer-lasting electrochemical performance.

One method for promoting particle growth, especially at lower temperatures, is through the use of molten fluxes, which have been applied in the synthesis of a variety of material systems.[41,42] The choice of flux can strongly influence the shape and morphology of the growing particles. Naturally, molten fluxes have also been adopted to modify the particle morphology of cathode materials during synthesis.[43 47] However, while these methods have shown promise, their viability for larger scale synthesis of cathode materials is questionable as several additional processing steps are introduced into the synthesis procedure to recover the pristine cathode material from the reaction mixture (such as deagglomeration, washing, and post-annealing).[48] Processes such as washing to dissolve and separate the flux from the cathode material can negatively affect the electrochemical properties of the cathode material even if the desired morphology is achieved.[49,50] To alleviate this issue, it may be possible to choose fluxes of desirable composition, which can be added to the reaction mixture in low amounts and act as a flux during annealing and also react with the cathode material to introduce favourable dopants into the structure. This would enable the modification of both the material's structure and the microscale particle morphology without introducing any additional processing steps into the synthesis procedure.

Hence, the concept of a dual-purpose, sacrificial flux, which could modify the particle morphology during annealing, and also decompose and react with the host material in the latter stages of synthesis, is proposed here. This was achieved by the addition of ammonium tungstate to the precursor reaction mixture. Tungsten (W) has been shown to be a dopant of great promise for LNO and Ni-rich cathode materials in general.[51 53] Besides influencing particle morphology, several studies have also shown that the incorporation of various dopant elements can also influence the surface and/or structural stability of these materials.[54 62] As the tungstate flux has a low melting point ($\theta_m \approx 300$ °C), it is expected to melt during synthesis and distribute on the precursor material particles during the pre-annealing stage. At higher temperatures, the tungstate can react and introduce W into the LNO structure.[63] In this study, the structural implications of tungsten doping in LNO prepared by this method and its influence on electrochemical performance are described. The addition of ammonium tungstate to the precursor mixture influences both the morphology and structural stability of the cathode material during synthesis, while the substitution of small amounts of Ni with W in the LNO structure brings benefits to electrochemical performance and structural stability during (de-)lithiation.

Experimental

Synthesis

Samples were synthesised from suitable amounts of $Ni(OH)_2$ (BASF SE), $LiOH \cdot H_2O$ (BASF SE) and $(NH_4)_{10}H_2(W_2O_7)_6$ (ammonium tungstate, Sigma Aldrich), with a precursor stoichiometry assuming W substitutes at the Ni site and $n(Ni + W) : n(Li) = 1 : 1.01$. The powder precursors were blended to ensure homogeneity and transferred to an alumina crucible. The samples were then annealed under O_2 flow. The samples were heated to 300 °C for 10 h with a ramp rate of 3 °C min^{-1}, before the temperature was raised to the desired annealing temperature and held for 6 h.

Elemental analysis

The Li, Ni, W and O contents of the samples were determined *via* inductively coupled plasma-optical emission spectroscopy (ICP-OES) using a Thermo Fischer Scientific iCAP 7600 DUO. The mass fraction was determined from three independent measurements. About 10 mg of the samples was dissolved in 6 mL of hydrochloric acid and 2 mL of nitric acid at 353 K for 4 h in a graphite oven. The digestions were diluted, and analysis of the elements was accomplished with four different calibration solutions and an internal standard (Sc). The range of the calibration solutions did not exceed a decade. Two or three wavelengths of elements were used for calculation. The O content was analysed with the method of carrier gas hot extraction (CGHE) using a commercial oxygen/nitrogen analyser TC600 (LECO). The O concentration was calibrated with the certified standard KED 1025, a steel powder from ALPHA. The standards and samples were weighed with a mass in the range from 1 to 2 mg together with 5 mg of graphite in Sn crucibles (9–10 mm) and wrapped. Together with a Sn pellet, the wrapped samples were put into a Ni crucible and loaded in an outgassed (6300 W) double-graphite crucible. The measurements took place at

5800 W. The evolving gases, CO_2 and CO, were swept out by He as inert carrier gas and measured using infrared detectors.

Electron microscopy

Scanning electron microscopy (SEM) and energy-dispersive X-ray spectroscopy (EDX) were carried out at 10 kV using a LEO-1530 electron microscope (Carl Zeiss AG) with a field emission source. Particle size distributions were determined using the software ImageJ.[64]

Transmission electron microscopy (TEM) of the samples was performed on a Themis Z (ThermoFisher Scientific) double-corrected transmission electron microscope operated at an acceleration voltage of 300 kV. Lift-out samples (TEM lamella) were prepared on a STRATA (FEI) dual-beam system equipped with a gallium ion source. The samples were milled at 30 kV, followed by final polishing at 2 kV to reduce the surface damage layer. Prior to the milling, the sample surface was protected by deposition of a carbon layer. Scanning TEM (STEM) images were collected using a high-angle annular dark-field (HAADF) detector. Elemental distribution was studied from EDX maps collected using the Super-X Detection System available at Themis Z.

X-ray diffraction (XRD)

Synchrotron XRD. Synchrotron XRD data were collected on the MSPD beamline at the ALBA Synchrotron, Spain.[65] This beamline utilises a one-dimensional silicon-based position-sensitive MYTHEN detector in Debye–Scherrer geometry, enabling fast data acquisition with excellent statistics and high angular resolution. Data were collected at a wavelength of $\lambda = 0.62001(8)$, determined using a NIST Si 640c SRM, in the angular range $0.4° < 2\theta < 57°$ ($Q \approx 0.0708$–9.671 Å^{-1}). The instrumental contribution to the peak broadening was obtained by measuring a crystalline $Na_2Ca_3Al_2F_{14}$:CaF_2 (NAC) sample as a line broadening reference. An overall acquisition time of 5 minutes was used to measure each sample, which was packed in 0.5 mm borosilicate glass capillaries. Sample absorption was calculated based on a measured packing density of 1.66 g cm^{-3} ($\approx$35% packing fraction).

Rietveld refinement was performed using GSAS-II.[66] The scale factor, zero shift, and crystallite size/strain broadening parameters were allowed to vary. A fixed background was fitted to the data using a Chebyshev polynomial function with 11 terms. In the structural model, the unit cell parameters, the oxygen z-coordinate and the atomic displacement parameters (isotropic, U_{iso}) for each site were refined. Atoms occupying the same site were constrained to have the same U_{iso}, and site occupancy factors (SOFs) were constrained such that each site remained fully occupied. Previous studies have shown that systematic errors in refinement of XRD data from layered cathode materials can be corrected by the optimal choice of form factors.[67] Hence, neutral atomic form factors were chosen for the Li and Ni sites in the structural models, while the ionic O^{2-} form factor was used for the O site.

***In situ* variable temperature XRD.** Powder XRD was performed using a laboratory diffractometer optimised for *in situ* measurements.[68] The diffractometer is equipped with a molybdenum microfocus rotating anode (Mo-K$\alpha_{1,2}$) and a Pilatus 300 K-W area detector. The sample was heated in a home-built gas flow furnace for *in situ* XRD based on the design of Chupas *et al.*[69] Powders were packed into sapphire capillaries with diameter 1.016 mm, which were used instead of borosilicate glass to minimize chemical reaction between the sample and capillary. To ensure accurate measurement of the sample temperature, a thermocouple is placed within the sapphire capillary adjacent to the powder sample. The dwell and ramping temperatures were calibrated *vs.* the unit cell volume of an Al_2O_3 standard measured under the same heating profile.[70]

Rietveld refinement was carried out sequentially against the *in situ* diffraction patterns. The zero offset and instrumental contribution to peak broadening were determined by measurement of a LaB_6 660b standard reference material. A Chebyshev polynomial function with 14 terms was used to fit the background profile caused by the sapphire capillaries. The background function as well as the sample displacement parameters were refined for the first *in situ* dataset and then fixed throughout, while other structural and atomic parameters were allowed to vary as discussed above.

Electrochemical characterisation

Electrode fabrication. Electrodes were prepared by casting an *N*-methyl-2-pyrrolidone (99.5%, Merck) slurry containing the active material, polyvinylidene difluoride (PVDF, Solvay) and Super C65 carbon black (TIMCAL) onto 0.03 mm-thick aluminium foil. The electrode tape was dried under vacuum overnight at 100 °C and then calendared at a pressure of 14 N mm^{-1}. Circular electrodes of 12 mm diameter were punched out before and then transferred to a heated glovebox antechamber for final vacuum drying at 100 °C. Resultant electrodes had an areal loading of $\approx$6.0 mg cm^{-2} with a mass ratio of 94 : 3 : 3 (active material : PVDF : Super C65).

Cell assembly. CR2032 coin cells were assembled in an Ar-filled glovebox using a GF/A-type glass microfiber separator (Whatman), 0.6 mm-thick lithium foil anode (Albemarle, Germany) and 95 μL of LP57 electrolyte (1 M $LiPF_6$ in 3 : 7 wt% ethylene carbonate : ethyl methyl carbonate, BASF SE).

Electrochemical testing. Coin cells were cycled in a controlled environment at 25 °C, using a Series 3600 Primary Cell Test System (MACCOR Inc.). The cells were cycled galvanostatically, firstly charged to 4.3 V *vs.* Li$^+$/Li at C/10, followed by 15 min of constant voltage (CV) charging (or a shorter period if the charging current dropped below C/20), and discharged to 3.0 V *vs.* Li$^+$/Li at a rate of C/10, with a 5 min rest step after each charge or discharge. After the first 5 cycles, the charging and discharging rates were set to C/4 and C/2, respectively, and the duration of the CV step at 4.3 V was set to 10 min. The applied current was calculated based on the active mass of each electrode, assuming a practical capacity of 1C = 225 mA g^{-1}. For long-term cycling data, several identical cells were prepared, and their average capacity is reported with error bars.[71] Electrochemical impedance spectroscopy (EIS) was measured using

a VMP3 multichannel potentiostat (BioLogic) over a frequency range of 100 mHz to 1 MHz with a voltage amplitude of 7 mV.

***Operando* XRD.** For *operando* XRD studies, coin cells were constructed utilising drilled CR2032 casings with a glass window 6 mm in diameter and 160 μm in thickness. Cells were cycled at a rate of C/10 using a Gamry Interface 1000 potentiostat, while XRD patterns were collected simultaneously using a STOE Stadi-P diffractometer with the Mo anode. Diffraction data were collected in the range $6^\circ < 2\theta < 37^\circ$ with a collection time of 10 minutes per pattern.

Results and discussion

Physical properties

A series of W-doped LNO samples were prepared by addition of ammonium tungstate to the precursor mixture during synthesis. Several samples were synthesized with 1 mol% W content but with varying annealing temperature, and samples were also prepared with 0.5, 1.5 and 5 mol% W at an identical annealing temperature of 700 °C. Electron microscopy was used to reveal the influence of synthesis temperature and W content on the particle morphology of the materials, see Fig. 1a–i. At identical annealing temperature, the introduction of W results in smaller primary particles. This suggests that the tungsten precursor passivates the surface, thereby hindering particle growth. Moreover, the introduction of W into the structure results in the formation of elongated primary particles, particularly evident in the samples prepared at 700 °C. Similar behaviour has also been observed in tungsten modified Ni-rich NCM materials.[52,72,73] WO_3-modified materials in particular were found to exhibit radially aligned grains.[74] While increasing the synthesis temperature to 750 °C, the elongated grain-like morphology is retained. Further temperature increase results in a morphology more closely resembling the granular one of the reference sample, albeit with an increase of the primary particle size, which is pronounced significantly in the 900 °C sample. The distribution of particle sizes for samples prepared at various temperatures is presented in Fig. 2. Elemental mapping using EDX, see Fig. 1j, also suggests that W has been distributed homogeneously amongst the secondary particles.

Cross-sectional STEM images taken from selected samples are presented in Fig. 3. A clear variation in primary particle size distribution from the interior to the surface of the secondary particles was found in the W-containing samples. Comparing the 1 mol% W samples, the particles at the surfaces of the 700 °C and 800 °C samples grow into a more elongated shape compared to the interior, which may be related to a gradient of tungsten concentration from the core to the surface of the secondary particles.[74] When the synthesis temperature is increased to 900 °C, a more uniform distribution of larger primary grains is found. Meanwhile, increasing the W content to 5% inhibits grain growth significantly, resulting in a morphology in which it is difficult to distinguish individual grains. This suggests that at elevated temperatures, thermally induced particle growth dominates and counteracts the morphological modifications introduced by the presence of

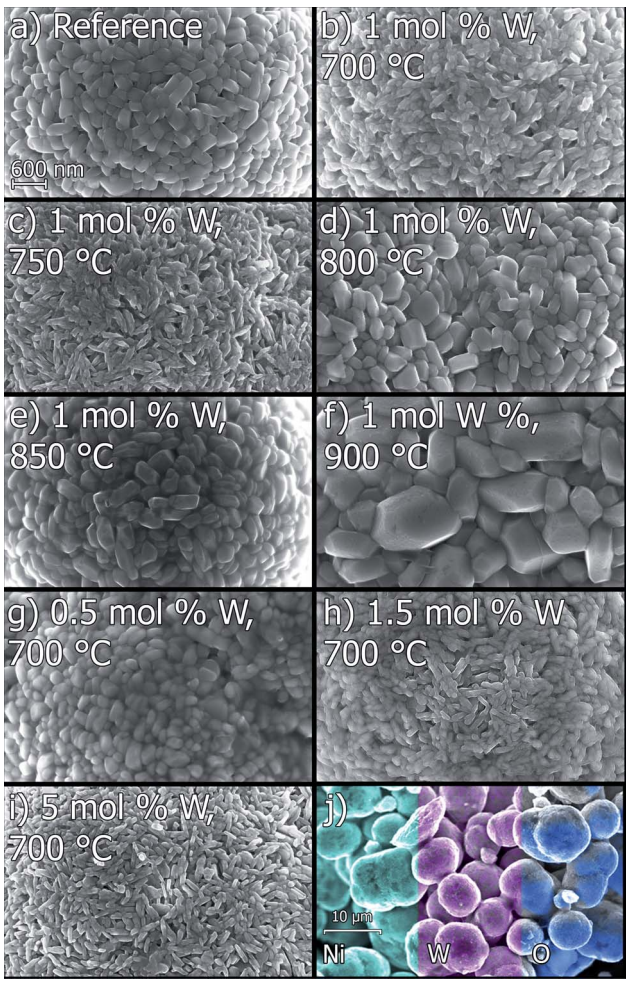

Fig. 1 (a i) SEM images collected at 20 000× magnification ((a) (i) use the same scale bar), comparing the primary particle morphology of the W-doped LNO samples. (j) Elemental distribution colour map determined from EDX of the 1 mol% W sample synthesised at 700 °C. Individual EDX spectra are presented in Fig. S5.†

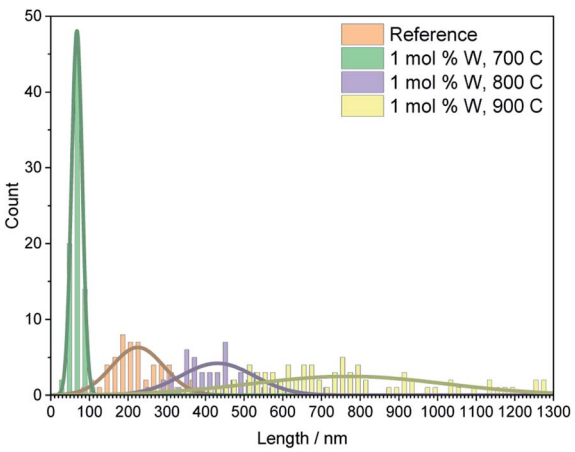

Fig. 2 Primary particle size distribution determined from the SEM images in Fig. 1.

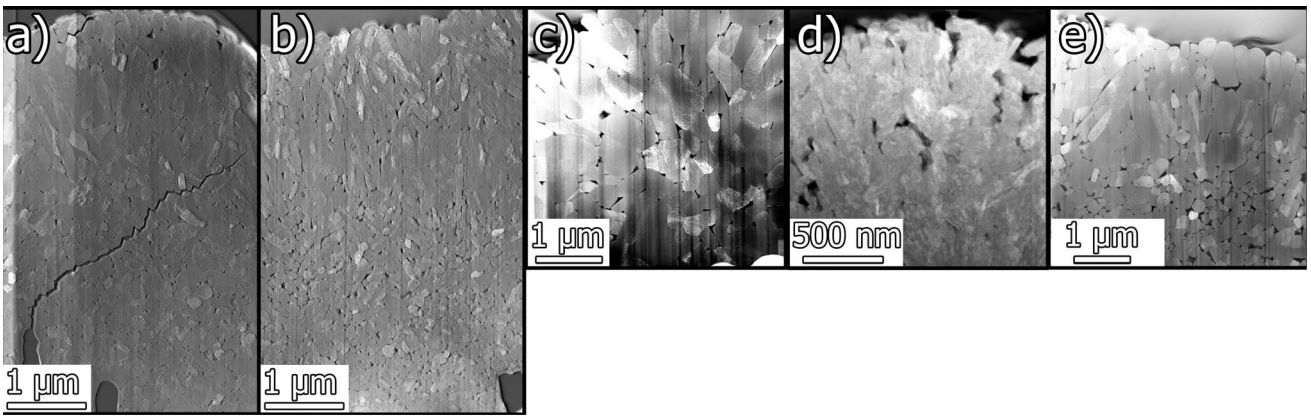

Fig. 3 FIB cross-sectional TEM images showing the interior primary particle morphology of W-doped LNO samples (a–d): (a) 1 mol% W, 700 °C; (b) 1 mol% W, 800 °C; (c) 1 mol% W, 900 °C; (d) 5 mol% W, 700 °C; and (e) reference LNO.

tungsten. TEM-EDX was also used to provide information on the elemental distribution within secondary particles for selected samples, see Table S1 and Fig. S1.† The measured W content is much lower than the expected nominal concentrations, suggesting that the concentration of W is larger in primary particles close to the outer edge of the secondary particles. The TEM-EDX images also suggest an enrichment of tungsten at the grain boundaries between primary particles, which is however only evident for samples prepared at temperatures higher than 700 °C.

Synchrotron XRD data were collected from the W-doped samples to study the bulk composition and structure of the materials, see Fig. 4. The introduction of tungsten into the structure results in significant broadening of the LNO Bragg reflections compared to the reference sample, as highlighted in the left insets, a consequence of the smaller primary crystallites as observed in the electron microscopy. Meanwhile, synthesising the material at higher temperature results in the formation of minor impurity phases, highlighted most obviously in the 8° < 2θ < 14° region. Some of these reflections could be indexed to Li_2CO_3, a common surface impurity produced by reaction of

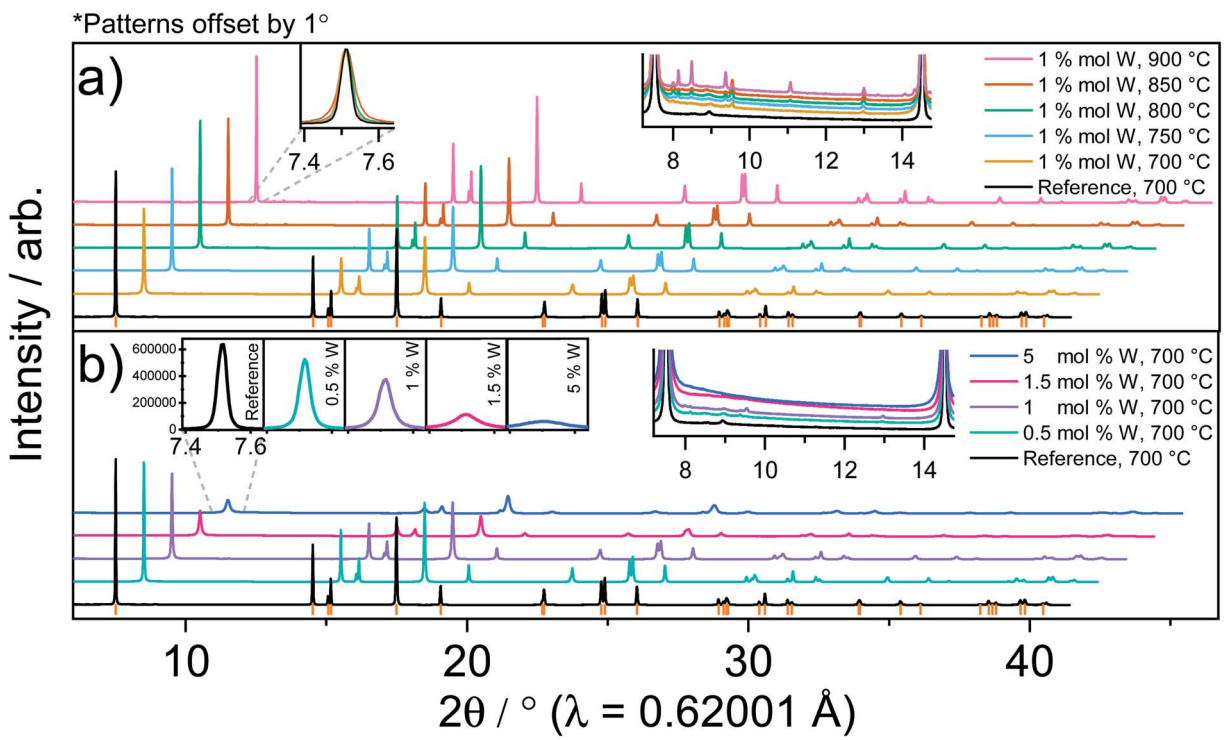

Fig. 4 Synchrotron XRD data collected from the W-doped LNO materials, prepared with varying (a) synthesis temperature and (b) tungsten content. Insets of figures (a) and (b) compare the profile of the 003 reflection, as well as the region between the 003 and 101 reflections where impurities are expected to be observed.

residual surface lithium during handling after high temperature synthesis, while reported structures of Li_xWO_y compounds did not match the peaks observed.[50,75] ICP-OES was also used to investigate the elemental composition of the samples, see Table S2.† The measured tungsten content appears consistent with the expected nominal concentrations, and with increasing temperature a decrease in the Li content is observed, which could be attributed to lithium loss at high temperatures.

The stoichiometry of the precursors used in the synthesis of W-doped LNO was calculated assuming that W occupies the 3a (Ni) site in the LNO lattice. In principle, the distribution of W amongst the primary particles may not be homogeneous, and cannot be resolved by XRD, which is an averaging bulk analysis technique. The SEM/EDX results show that the W distribution appears homogeneous at the surface of the secondary particles, while the cross-sectional TEM images pointed towards a stronger effect of W on the primary particles located towards the surface based on their observed size and shape, and also showed a W enrichment at the surface of primary particles and in grain boundaries. XRD offers reasonable elemental contrast between Ni ($Z = 31$) and W ($Z = 74$), which have corresponding X-ray scattering cross sections of $\sigma_a(\mathrm{Ni}) = 9.7457$ barns per atom and $\sigma_a(\mathrm{W}) = 305.29$ barns per atom, respectively.[76] Hence, synchrotron XRD is suitable to verify whether, on average, W does nonetheless modify the bulk crystal structure of LNO. Tungsten in an octahedral site exhibits an ionic radius of $r(W^{6+}) = 0.6$ Å, significantly lower than that of monovalent lithium, with $r(Li^+) = 0.76$ Å, but also slightly larger than trivalent nickel, with $r(Ni^{3+}) = 0.56$ Å.[77] Considering ionic radii alone, occupation of either the 3a (Ni) or 3b (Li) is plausible, however the substitution of monovalent lithium with high-valence cations such as hexavalent tungsten (W^{6+}) would create highly charged point defects in the layered structure that are energetically unlikely. Previous simulation studies of doping into Ni-rich cathode materials predict a positive heat of formation during substitution of the 3b site, while a negative heat of formation results from doping the 3a site,[78] which implies that substitution of Ni is indeed thermodynamically more favourable. As XRD is not well suited to probing Li, three models were tested by applying structural models with Ni or W placed on the 3a and 3b sites, or both, in the structure. In this initial refinement, the occupancy of each element in the 3a and 3b sites was allowed to vary, or fixed to zero accordingly, each site was constrained to be fully occupied, and the total tungsten content was constrained as per the molar ratio determined from ICP. A hexagonal α-$NaFeO_2$-type structure with space group $R\bar{3}m$ was refined against the data collected from the 1 mol% W $LiNiO_2$ sample synthesised at 700 °C, see Table S3.† Models II and III converge towards unsatisfactory ADP values of the 3a and 3b sites, while model III also produced a negative SOF for W in the 3b site. Previous studies utilising concurrent refinement of structural models against both neutron and synchrotron data suggest reasonable ADP values of $U_{iso}(\mathrm{Li}) = 0.0119$ and $U_{iso}(\mathrm{Ni}) = 0.00374$ (reported as $B_{Li} = 0.943$ Å^2 and $B_{Ni} = 0.295$ Å^2).[79] Hence, the physically meaningful model is suggested to be model I, with W only on the 3a site, which also led to the best quality of fit. This model was then used as a starting point for refinements against diffraction data collected from the remaining samples. The occupancy of W on the 3a site, and the total occupancy of Ni on the 3a and 3b sites were constrained in accordance with the elemental composition determined by ICP-OES measurements. Using this model, a satisfactory agreement between the observed and calculated structural data was achieved, including the high-angle range. An example of the typical quality of fit is depicted in Fig. 5.

The refined structural parameters determined by fitting this model to the diffraction data collected from each sample are presented in Table 1. Fig. 6a shows the evolution of the parameters with increasing W content. The unit cell volume increases with higher tungsten content compared to the reference sample, and so does the a unit cell parameter, which is expected given the larger ionic radius of W^{6+} compared to Ni^{3+}. The c/a ratio remains relatively constant at low doping levels but is decreased considerably in the 5 mol% W sample, which was also found to have a higher Ni off-stoichiometry. This suggests that low levels of W-doping do not significantly affect the rhombohedral distortion of the LNO structure, consistent with previous reports of W-doping in this system.[52] The Ni : Li off-stoichiometry also varies with increasing W content, which can be attributed to the formation of Ni^{2+} in the structure to compensate for the hexavalent W^{6+} to maintain charge balance. This is clearly evidenced in the off-stoichiometry observed for the samples prepared at 700 °C, which all show an increase compared to the reference sample. With 0.5 mol% W introduced, the Ni off-stoichiometry increases by a factor of roughly 1.5 (or 3 times the W mol%) compared to the reference sample, 0.028(1) compared to 0.017(1), and this trend is further observed as the W content is increased to 1 mol% and then 1.5 mol%. This relation between the fraction of Ni on the Li site and the W mol% allows us to suggest a formula unit $Li_{1-3x}Ni_{3x}(Ni_{1-3x}W_x)O_2$, where some amount of vacancy is present on the Ni site to respect charge balance. The grey trend line drawn in Fig. 6a shows good agreement between the refined Ni on the Li site and what is predicted by the above formula. This is

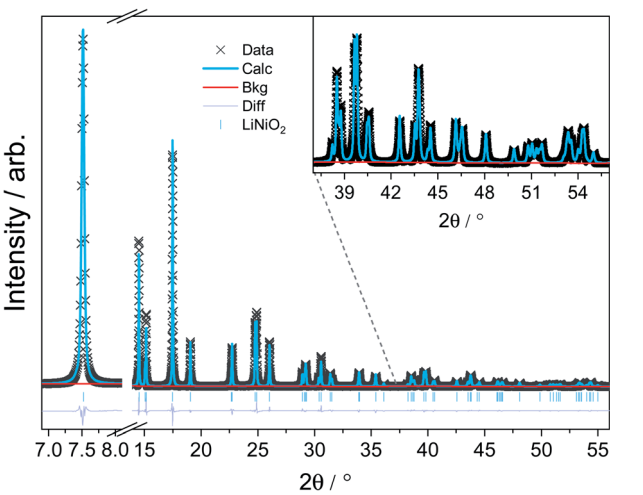

Fig. 5 Rietveld refinement profile of synchrotron XRD data collected from a 1 mol% W LNO sample synthesised at 700 °C.

Table 1 Refined structural parameters of W-doped LNO samples. W content is constrained as obtained by ICP and Ni content on both sites as well (Ni_{3a} + Ni_{3b} Ni_{ICP}). Finally the Li site is constrained to be fully occupied

W/ mol%	Temp./ °C	a/Å	c/Å	V/Å^3	c/a ratio	Ni on Li site	z of O	U_{iso} 3b (Li) × 10 ^{2}	U_{iso} 3a (Ni) × 10 ^{2}	U_{iso} 6c (O) × 10 ^{2}	R_F/%	R_w/%
0	700	2.87681(2)	14.1982(10)	101.762(1)	4.93539(1)	0.017(1)	0.25831(8)	0.009(1)	0.003(1)	0.0100(3)	1.45	8.91
0.5	700	2.87762(2)	14.1962(1)	101.806(1)	4.93332(1)	0.028(1)	0.2579(6)	0.0110(7)	0.00220(6)	0.0102(2)	1.44	6.75
1	700	2.87881(5)	14.2027(2)	101.936(3)	4.93354(2)	0.037(1)	0.25775(6)	0.0090(6)	0.00278(6)	0.0113(2)	1.49	6.36
1.5	700	2.87879(8)	14.1967(4)	101.891(5)	4.93149(4)	0.047(1)	0.2587(1)	0.0027(8)	0.00839(1)	0.0173(4)	2.52	7.16
5	700	2.8861(2)	14.2095(1)	102.500(1)	4.9235(1)	0.138(1)	0.2575(2)	0.0054(8)	0.0042(2)	0.0182(6)	4.11	11.57
1	750	2.87810(2)	14.2037(1)	101.893(1)	4.93509(1)	0.031(1)	0.25794(6)	0.0107(7)	0.00326(7)	0.0122(2)	1.51	6.65
1	800	2.87984(2)	14.2098(1)	102.060(1)	4.93422(1)	0.047(1)	0.25783(7)	0.0101(7)	0.00228(7)	0.0110(3)	1.55	7.85
1	850	2.88014(3)	14.2113(1)	102.092(2)	4.93422(1)	0.047(1)	0.25783(7)	0.0089(7)	0.00379(7)	0.0126(3)	2.1	7.69
1	900	2.88167(2)	14.2061(1)	102.164(1)	4.92982(1)	0.057(1)	0.25789(8)	0.0101(7)	0.00263(8)	0.0121(3)	1.69	8.84

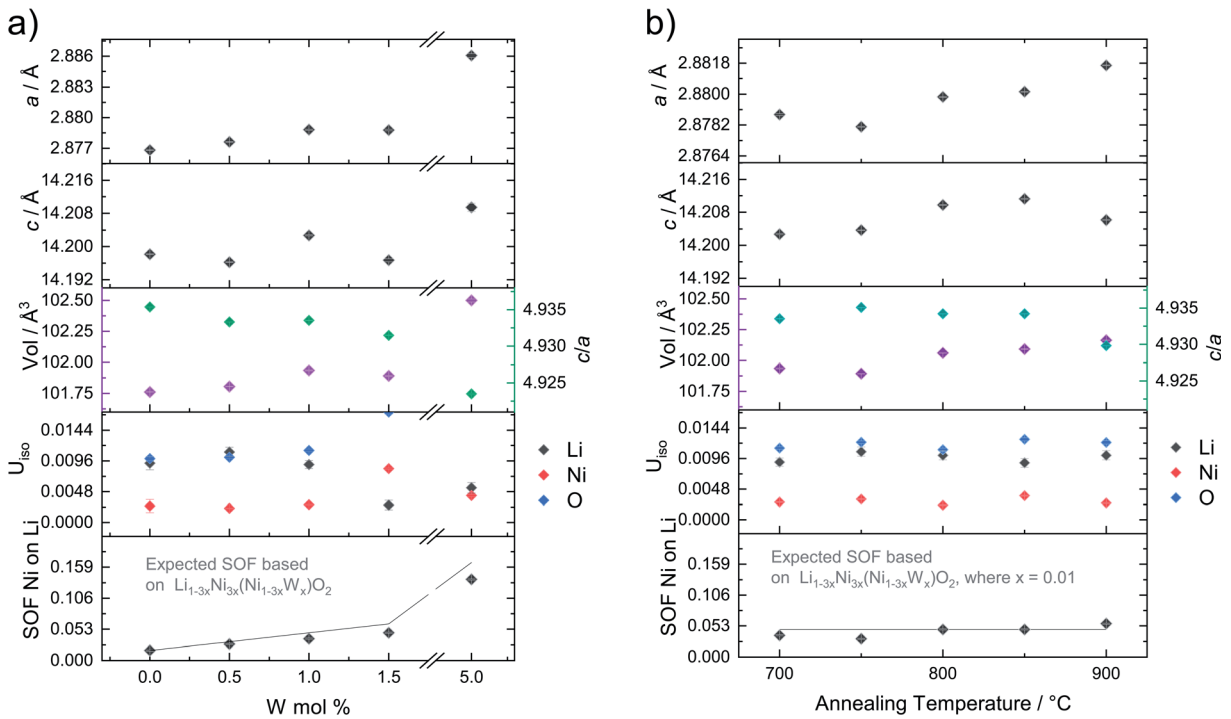

Fig. 6 Refined structural parameters of the W-doped LNO samples for (a) varying tungsten content and (b) synthesis temperature.

further supported by a decrease in the ADP of the Li site, which suggests the presence of increased electron density on this site, as a result of the increasing Ni : Li off-stoichiometry at higher W-doping. Similar results were recently found by Sun *et al.* for the introduction of other high-valent cations in $Li[Ni_{0.91}Co_{0.09}]O_2$, including Mo^{6+} and Ta^{5+}.[80] However, it should be noted that the above formula unit is not the only possibility; for example, one could also have $Li_{1-1.5x}Ni_{1.5x}(Ni_{1-2.5x}W_x)O_2$. While the previous formula unit provides a better fit to the refinement results, the fact that higher concentrations of W were detected at the grain boundaries, and the subsequent uncertainty on the value of x (W) that actually migrates into the bulk of the primary particles, does not allow us to settle firmly on a unique formula unit. Further characterization beyond what is reported in this paper (EXAFS, Li NMR, *etc.*) will be used to further confirm these formula units. It should finally be noted that, while we cannot settle on a unique formula unit based on XRD, we find a clear correlation between the amount of W on the 3a site and amount of Ni migrating to the 3b site; this is indeed in agreement with reports suggesting that W^{6+} induces a less layered and more rock salt-type structure.[81]

Meanwhile, the unit cell parameters are observed to increase for samples annealed at higher temperatures, see Fig. 6b. The conventional synthesis temperature of pristine LNO is 700 °C, as higher temperatures accelerate the decomposition of the material, leading to higher off-stoichiometry.[82] At constant W content (1 mol%), the Ni : Li off-stoichiometry increases from 0.037(1) at 700 °C to 0.057(1) at 900 °C. The c/a ratio also does not deviate significantly from the value of the reference sample, ≈4.935, except for the sample synthesised at 900 °C, where the ratio drops to ≈4.930. This behaviour suggests that doping with a small amount of W can help to stabilise the LNO structure

during synthesis at temperatures as high as 800 or 850 °C. On the other hand, increasing the W content substantially, such as in the 5 mol% W sample, reduces layering in the structure as expected.[81]

High temperature stability. While LNO is conventionally synthesised at 700 °C, it has been demonstrated that the material already begins to slowly decompose at this temperature.[83] To investigate whether W influences the high temperature stability of this material, *in situ* XRD was employed to study the decomposition of as-synthesised materials in air: reference LNO and 1% W-doped LNO synthesised at 800 °C. The materials were heated sequentially to 600 °C, 700 °C and 800 °C for two hours at each temperature while collecting XRD data, see Fig. 7. The most obvious shift in the position of the reflections is attributed to thermal expansion with varying temperature. However, there is also significant structural evolution observed during each temperature dwell, which is attributed to chemical decomposition.

The results of Rietveld analysis are shown in Fig. 8 below, and an example of the quality of fit achieved during the experiment is shown in Fig. S2.† The change in unit cell volume is clearly accelerated at higher temperatures. To compare the behaviour in different regions, the rate of change of cell volume per unit time (dV/dt [Å^3 min^{-1}]) was determined using linear fitting to the temperature dwell regions, as labelled in Fig. 8a. At 600 °C, the cell volume of both samples does not increase significantly. When the temperature is increased to 700 °C, the rate of volume change for both samples increases significantly to 0.00134 Å^3 min^{-1} and 0.00248 Å^3 min^{-1} for the W-doped and reference sample, respectively. At 700 °C, a clear improvement in the structural stability of the W-doped material is already demonstrated. At 800 °C, this is further exacerbated, with the rate of change of cell volume of the W-doped material increasing to just 0.00146 Å^3 min^{-1}, compared to a much faster increase to 0.00338 Å^3 min^{-1} for the reference LNO sample. The observed change in cell volume is largely attributed to the change in a parameter, which increases substantially with temperature, and more rapidly during the higher temperature dwells. The c parameter meanwhile does not vary significantly at 600 °C or 700 °C, but decreases rapidly at 800 °C. Previous studies investigating the decomposition of LNO have attributed this to the fact that the change in a is largely dependent on the reduction of Ni^{3+} to Ni^{2+} in the Ni layer, while the c parameter remains relatively constant as the loss of lithium from the Li layer is compensated by migration of Ni^{2+} into the layer.[40] Comparing the c/a ratio of the two samples during heating, Fig. 8b, also reflects this behaviour, with a much larger change observed for the reference LNO sample. After cooling, both the a and c parameters remain considerably larger than in the original material, indicating that the decomposition causes an irreversible structural change. The c/a ratio of layered oxide materials can provide an indication of the degree of layering in a material, with a value of 4.899 being observed for materials exhibiting ideal cubic stacking, while higher values, >4.95, suggest a more layered (rhombohedral) trait.[84] The c/a ratios of the LNO phases in this experiment show a clear downward trend during each temperature dwell. The W-doped sample exhibited an initial c/a ratio of ≈4.934 and ≈4.924 after cooling, compared to an initial value of ≈4.939 and ≈4.920 after cooling for the reference sample, further highlighting the increased irreversible decomposition of the pristine material compared to the W-doped material. This large structural change could be attributed to the loss of lithium from the structure at high temperatures, which is reinforced by the rapidly increasing occupancy of Ni on the Li site, see Fig. 8e. In conclusion, we shall note that the enhanced structural stability at high temperature is in good agreement with the formula units we reported above, which implies an average oxidation state of Ni lower than 3+, hence the possibility to increase the synthesis temperature without incurring into decomposition effects.

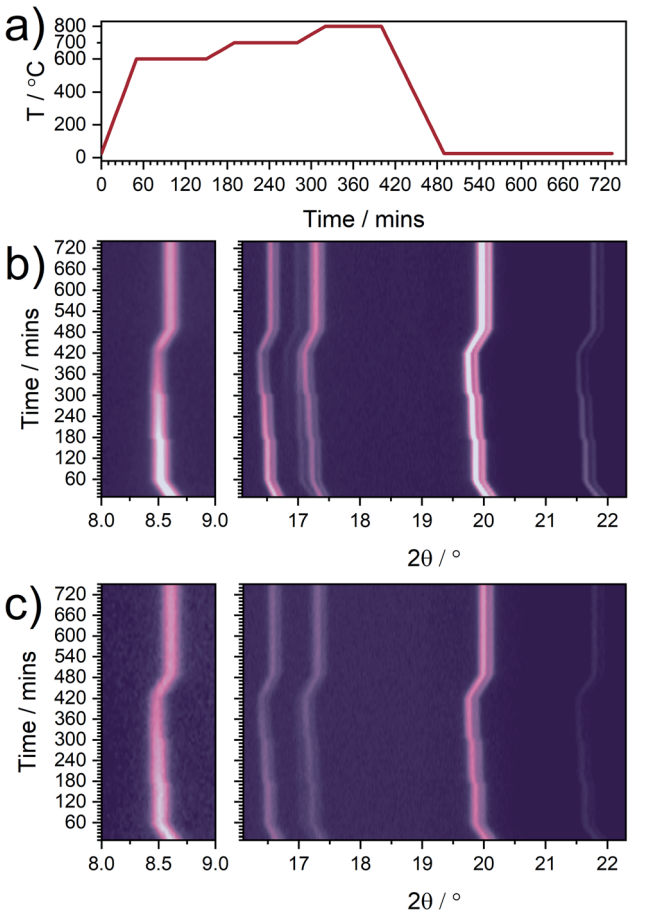

Fig. 7 (a) Temperature profile recorded during the *in situ* heating experiment. (b, c) Contour plots showing evolution of XRD data collected during heating of (b) reference LNO and (c) 1 mol% W-doped LNO.

Electrochemical measurements

The electrochemical performance of the W-doped LNO materials was evaluated. The observed voltage profiles of the different materials during the 2nd cycle, as a function of synthesis temperature and W content, are presented in Fig. 9a and c. Firstly, considering the 1 mol% W samples prepared at various temperatures, see Fig. 9a, it is evident that the specific charge and discharge capacity decrease as a function of

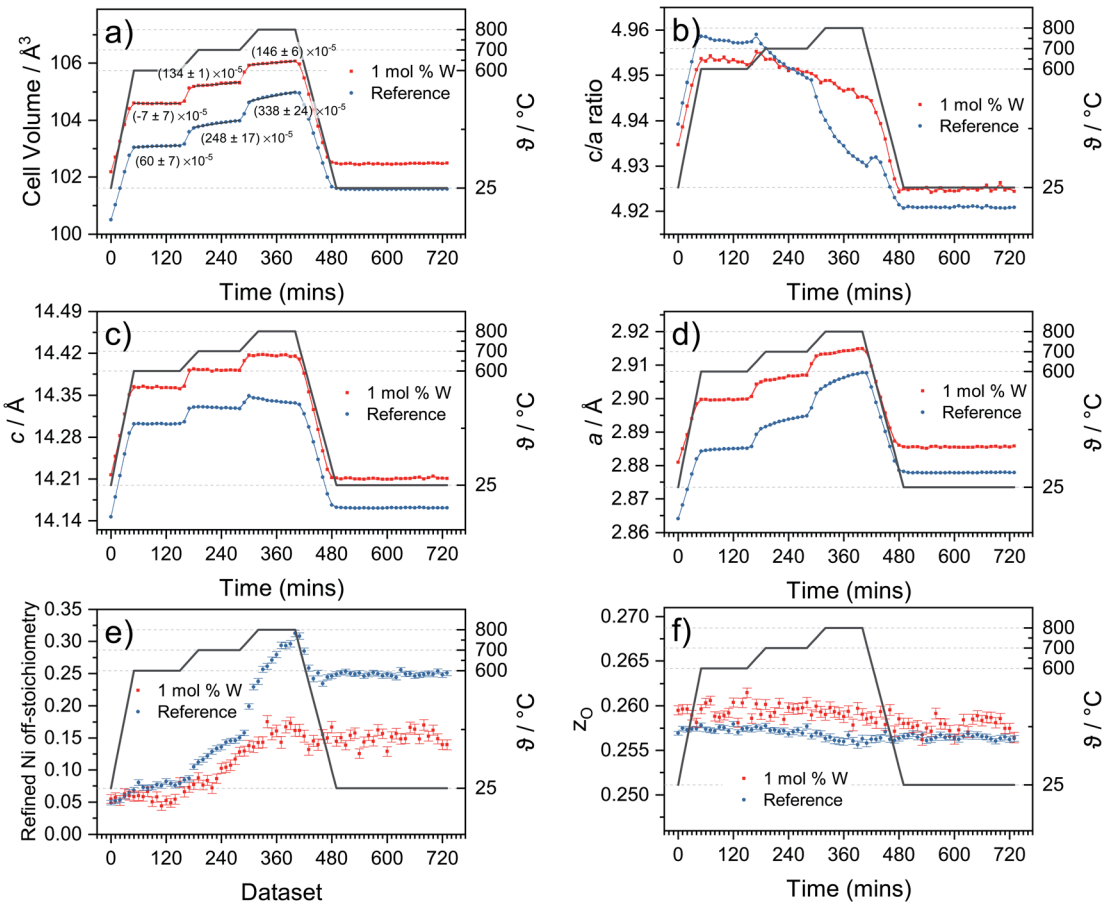

Fig. 8 Refined structural parameters of the LNO phases during the *in situ* heating experiment. Error bars are visible, the spread is greater than the size of the data points. (a d) Unit cell volume, *c*/*a* ratio, *a* and *c* parameters. In (a) the rate of change of cell volume (d*V*/d*t* in Å^3 min ^{1}) determined by linear fitting during each temperature dwell is also shown. (e) Site occupancy factor of Ni in the Li site. (f) Fractional atomic coordinate *z* of oxygen.

synthesis temperature. When cycled at C/10, the discharge capacity decreases from 214.4 to 179.9 mA h g^{-1} as the sample's synthesis temperature is increased from 700 to 900 °C, compared to 218.4 mA h g^{-1} for the pristine sample. This is consistent with the Rietveld refinement results discussed earlier, which suggests a higher Ni occupancy on the Li site with increasing temperature, thereby reducing the amount of Li available for electrochemical (de-)intercalation, which may be compounded with slower Li diffusion kinetics due to the larger particle sizes of the 800, 850 and 900 °C samples. A similar trend is observed with varying W content, where the 0.5, 1 and 1.5 mol% W samples deliver a specific discharge capacity of 215.1, 205.3 and 203.6 mA h g^{-1} respectively, in line with the refined lithium content observed in the XRD data. The voltage profiles also exhibit less pronounced plateaus, which can be seen more clearly by analysing the differential capacity plots shown in Fig. 9b and d. Several peaks corresponding to transitions between the hexagonal and monoclinic phases of LNO are observed, with peaks at ≈3.6, 4.0 and 4.2 V corresponding to the H1 → M, M → H2 and H2 → H3 transitions, respectively.[85] The most pronounced peaks are observed in the pristine LNO sample, while the peak intensities diminish with increasing W content for both charge and discharge, suggesting the doping of the Li site encourages solid solution-like behaviour in this system, which has been previously reported.[52,86,87] In particular, the minimum in the d*q*/d*V* plot corresponding to the stable composition $x = 2/5$ (at ≈3.98 V in charge) is readily destabilised by variations of W content or synthesis temperature, confirming that this feature is only visible in highly stoichiometric LNO samples.[88,89] The reduction in intensity is also accompanied by a shift in the average voltage of each of the features, highlighted in the zoomed plots of the 4.1 to 4.3 V region. Fig. 9b shows that there is an increase in the average potential of the H2 → H3 feature on both the charge and discharge cycles, which suggests it is caused by an increase in the equilibrium (de-)intercalation voltage of Li rather than cell polarization, which has been previously observed in doped LNO materials,[62] as well as in LNO with increasing off-stoichiometry.[89] The features corresponding to the H2 → H3 transitions in particular exhibit a much smoother gradient for the samples synthesised at 800 °C and above, which is characteristic of LNO with higher off-stoichiometry. Meanwhile, for the samples with increasing W content, see Fig. 9d, the same feature in the d*q*/d*V* plot shifts to higher voltage on charge and to lower voltage on

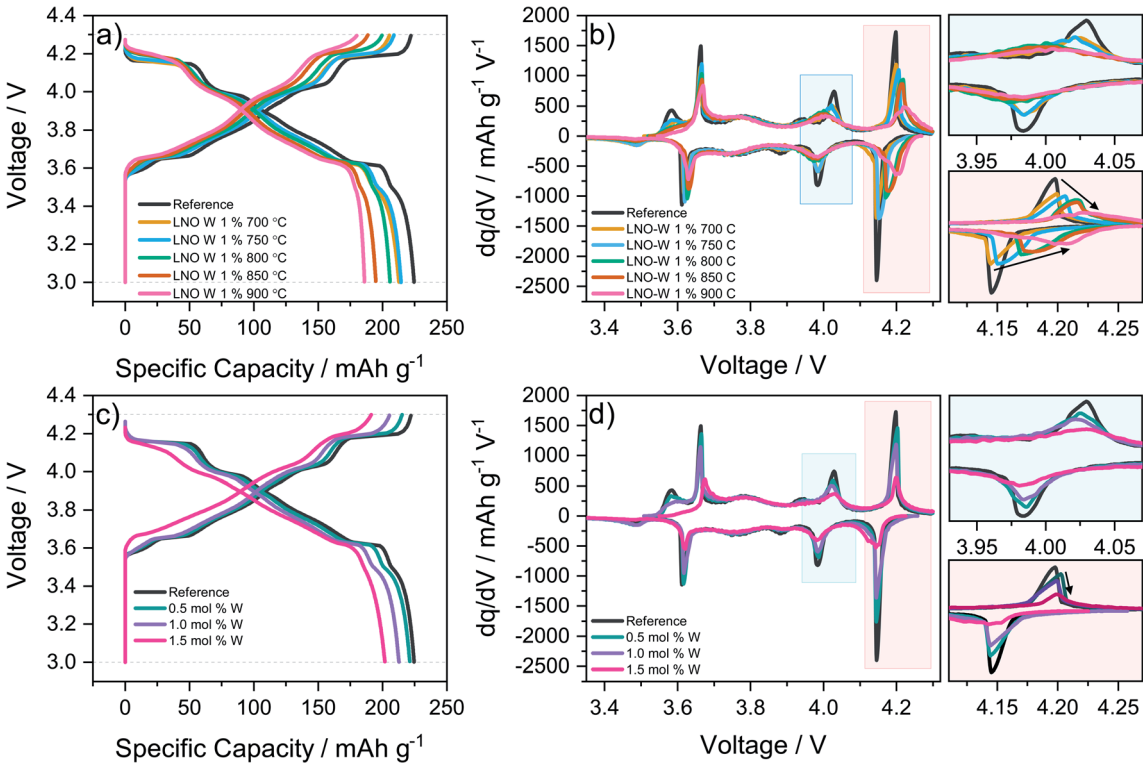

Fig. 9 (a, c) Voltage profiles observed during the first cycle and (b, d) differential capacity plots recorded during the 2nd cycle of coin cells utilising a W-doped LNO.

discharge, which implies that the higher W content induces an increased degree of polarization, either due to slower kinetics or an enriched rock salt-type layer at the surface of the particles. Closer inspection of the dq/dV plot in Fig. 9d also reveals that the typical kinetic feature observed at 3.5 V is not heavily affected by the increasing W content (at least at 0.5 mol% and

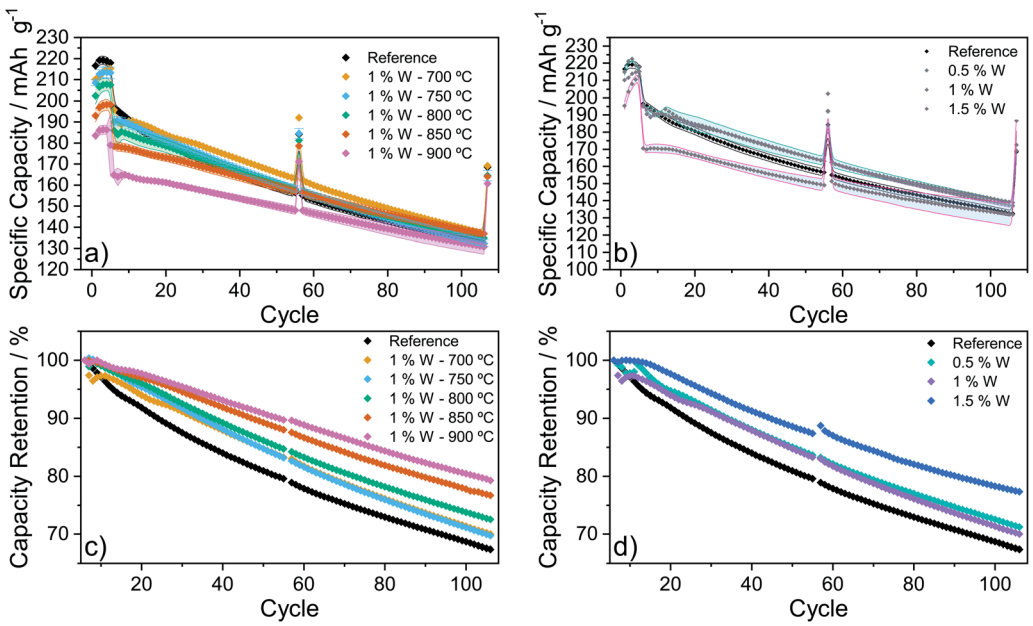

Fig. 10 Specific discharge capacity *versus* cycle number for (a) 1% W-doped LNO synthesised at various temperatures and (b) LNO synthesised at 700 °C with various W content. (c, d) Recorded capacity retention expressed as a percentage of the initial C/2 cycle capacity. Error bars are shown as shaded areas.

1 mol%), suggesting that diffusion kinetics is actually comparable at a low state of charge. On the other hand, the increased polarization is evident at high voltage and at the H2/H3 phase transition peak (4.15 V) in particular, pointing towards an inhibited phase transformation, as we will discuss in the following.

The long-term cycling behaviour of these samples was also investigated. Fig. 10 shows the average cell capacity as a function of cycle number recorded for cells utilising the W-doped LNO samples. The first five cycles were carried out at C/10, before the current was increased to C/2 for 50 cycles. After 50 cycles at C/2, a single cycle at C/10 was performed to investigate capacity retention compared to the initial cycles, before another 50 cycles at C/2 and a final 107th cycle at C/10. Despite the lower initial specific capacity discussed earlier, the W-doped samples exhibit excellent capacity retention. After 50 cycles at C/2, the 1 mol% W samples synthesised at 700–850 °C are all able to match or exceed the capacity of the reference sample, and continue to exceed its delivered capacity thereafter, see Fig. 10a. The sample prepared at 900 °C delivers instead a relatively lower capacity overall. After 100 cycles at C/2, the samples synthesised at 700–850 °C all deliver specific capacities ranging from 134.9–

Table 2 Specific discharge capacities (mA h g ^{1}) recorded during cycles performed at C/10 and relative capacities (%) observed on selected cycles

Sample	1st	56th	107th	106th/6th	6th/5th	55th/56th	106th/107th
0% W 700 °C	216.5 ± 1.9	184.9 ± 1.9	168.5 ± 1.8	67.3	90.2	84.9	78.5
1% W 700 °C	210.2 ± 0.2	192.0 ± 0.7	169.2 ± 1.4	73.8	91.1	84.9	81.0
1% W 750 °C	208.6 ± 1.4	184.5 ± 2.4	164.5 ± 2.4	69.7	89.1	85.7	80.6
1% W 800 °C	202.4 ± 4.0	181.3 ± 2.1	164.5 ± 1.7	72.5	90.1	86.9	82.0
1% W 850 °C	193.0 ± 3.0	178.6 ± 1.6	164.1 ± 1.4	76.7	90.0	87.9	83.3
1% W 900 °C	183.6 ± 2.2	171.2 ± 1.7	160.7 ± 1.8	79.3	92.1	86.4	81.3
0.5% W 700 °C	214.8 ± 1.7	192.4 ± 2.6	172.5 ± 5.4	71.2	89.6	84.8	80.5
1.5% W 700 °C	195.4 ± 2.2	202.4 ± 2.7	186.6 ± 5.8	77.3	80.2	73.7	70.7

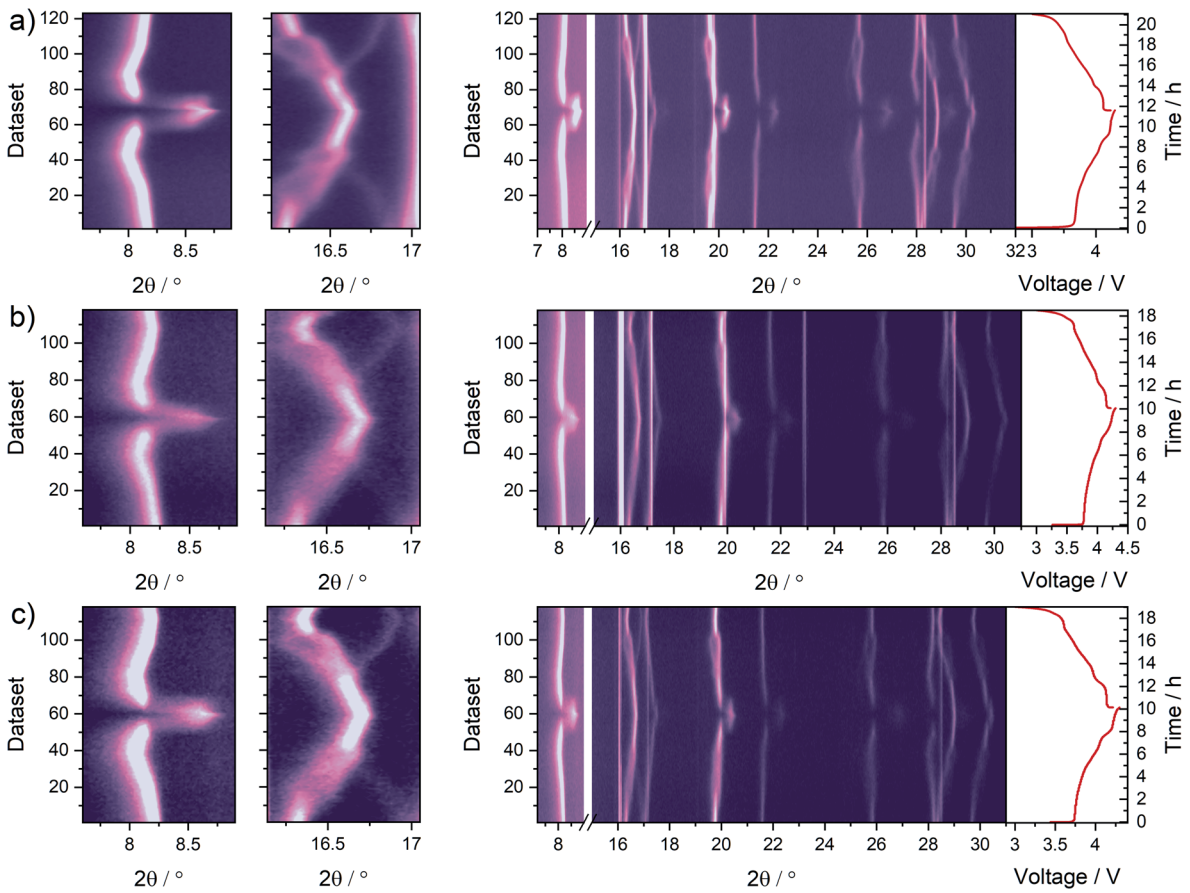

Fig. 11 Contour plots of XRD data collected during electrochemical cycling of (a) reference LNO, (b) 1 mol% W LNO synthesised at 700 °C and (c) 1 mol% W LNO synthesised at 800 °C. Corresponding voltage *vs.* time profiles are shown on the right.

135.9 mA h g^{-1}, while lower specific capacities of 130.8 mA h g^{-1} and 129.2 mA h g^{-1} are delivered by the 900 °C sample and reference sample, respectively. A final cycle at C/10 was carried out after cycling at C/2 to investigate the recoverable capacity of the materials. The reference sample exhibited a final capacity of (168.6 ± 1.8) mA h g^{-1}, while the capacities decreased from (169.2 ± 1.4) to (160.7 ± 1.8) mA h g^{-1} for the series of 1 mol% W samples synthesised at 700–900 °C, see Fig. 10. This capacity difference observed between the 106^{th} and 107^{th} cycles shows that all samples, besides the 1.5 mol% W sample, retain a higher relative capacity after 100 cycles at C/2 compared to the reference sample, implying that the reference sample exhibits a higher impedance build-up during cycling. Annealing at lower temperatures in particular, 700 or 750 °C, results in a small compromise to initial capacity, ≈5 mA h g^{-1}, while exhibiting higher capacity after the 10^{th} cycle and all cycles thereafter.

Comparing the samples with different W contents, Fig. 10b shows that while the 1.5 mol% W sample performs poorly, the 0.5 and 1 mol% W samples both exhibit good capacity retention when cycled at C/2, clearly exceeding that of the reference sample. These findings are highlighted more clearly in Fig. 10c and d, which show the recorded capacities expressed as a percentage of the initial capacity. An indication of the rate capability of the different materials can also be inferred by comparing the capacities delivered on the 5^{th}/6^{th}, 55^{th}/56^{th} and 106^{th}/107^{th} cycles, see Table 2, where the current was changed from C/2 to C/10. With the exception of the 1.5 mol% W material, all samples deliver a similar capacity retention of about 90% when the current is increased to C/2 at the 6^{th} cycle. However, at the 55^{th}/56^{th} cycle and 106^{th}/107^{th} cycle, most of the W-doped samples recover a few percentage points more capacity when the current is reduced from C/2 to C/10, indicating they have suffered less impedance build-up than the undoped sample. This is supported by impedance spectroscopy measurements carried out before and after cycling, see Fig. S4,† which suggest that the coin cells containing W-doped cathode materials exhibit reduced resistance as indicated by the smaller diameter of the semicircle observed in the measured high-to-medium frequency range.

Operando XRD

To investigate how the introduction of tungsten into the LNO structure influences the structural evolution that takes place during electrochemical cycling, *operando* XRD was used to characterise the cathode materials. Fig. 11 shows contour plots of the diffraction data collected during the first charge–discharge cycle at C/10 for a pristine LNO sample, and 1 mol% LNO synthesised at 700 °C and 800 °C. The structural evolution of LNO upon delithiation has been reported previously, and transitions through several hexagonal and monoclinic structures are expected, conventionally denoted as H1 > M > H2 > H3.[85,88,90] Visual comparison of the *operando* XRD data suggests that the introduction of W into the structure does not change the observed phase evolution. During the *operando* experiment, the undoped material delivered an initial specific charge capacity of 228.0 mA h g^{-1}, compared to 212.6 mA h g^{-1} and 204.3 mA h g^{-1} for the 1 mol% W samples prepared at 700 °C and 800 °C, respectively. All of the samples still exhibit the expected transitions, mentioned above, which is consistent with the differential capacity plots presented earlier. In particular, the graphs on the left of Fig. 11 highlight the $7.6° < 2\theta < 8.9°$ and $16° < 2\theta < 16.95°$ regions, which is where the 003_H and $10\bar{2}_H$/006_H reflections are observed, respectively. The splitting of the $10\bar{2}_H$ reflection is observed as the material undergoes a transition from the hexagonal to the monoclinic phase during (de-)lithiation. This transition has been well characterised in previous *in situ* XRD studies of LNO[85,90] and also observed in other layered cathode materials.[91,92] To compare the observed structural evolution quantitatively, Rietveld refinement was used to fit structural models to the diffraction data collected during cycling, see Fig. 12 and Table 3. An example of the quality of fit is presented in Fig. S3.† It is evident that the undoped reference sample exhibits a larger overall magnitude of structural expansion and contraction during cycling. This material exhibits a cell volume of 100.641(6) Å^3 at the discharged state, which reduces to 92.545(35) Å^3 as the cell reaches the charged state at 4.3 V. This corresponds to a 9.6% contraction in cell volume, compared to 7.7% and 7.3% for the

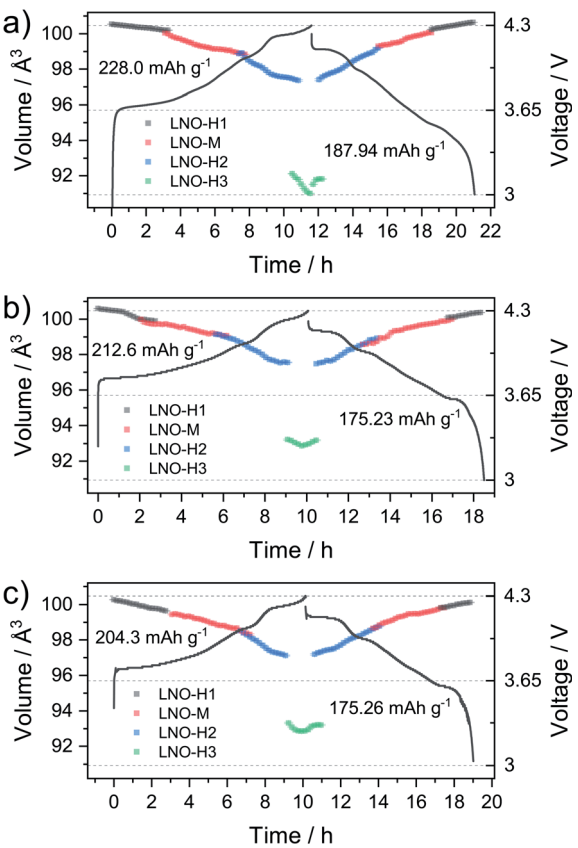

Fig. 12 Unit cell volumes of W-doped LNO observed during cycling, determined from Rietveld refinement of structures against XRD data gathered during the first cycle at C/10 rate, as shown in Fig. 11. (a) Reference LNO, (b) 1 mol% W LNO synthesised at 700 °C and (c) 1 mol% W LNO synthesised at 800 °C.

Table 3 Refined cell volumes of phases observed during a single charge cycle from 3 – 4.3 V *vs.* Li^+/Li

		Min		Max	
	Phase	Potential/V	Cell vol./Å^3	Potential/V	Cell vol./Å^3
Ref.	H1	3.7	100.199(15)	3	100.641(6)
	M (·3/2)	4.1	98.832(14)	3.7	99.998(10)
	H2	4.2	97.361(43)	4.1	98.903(15)
	H3	4.3	91.008(11)	4.2	91.915(15)
		Min		Max	
	Phase	Potential/V	Cell vol./Å^3	Potential/V	Cell vol./Å^3
1% W, 700 °C	H1	3.7	100.102(31)	3	100.597(14)
	M (·3/2)	4	99.070(24)	3.75	99.996(30)
	H2	4.2	97.467(34)	4	99.123(44)
	H3	4.3	92.868(29)	4.2	99.379(25)
		Min		Max	
	Phase	Potential/V	Cell vol./Å^3	Potential/V	Cell vol./Å^3
1% W, 700 °C	H1	3.7	99.640(21)	3	100.117(18)
	M (·3/2)	4	98.401(19)	3.75	99.461(23)
	H2	4.2	97.094(31)	4	97.933(38)
	H3	4.3	92.845(24)	4.2	93.668(46)

W-doped samples prepared at 700 °C and 800 °C, respectively, over the same voltage range. Comparing the difference in cell volume between the H2 and H3 phases is also significant as this two-phase transition is largely responsible for the poor cycle life observed in Ni-rich layered cathode materials.[11] In the reference sample, the minimum volume observed for the H2 phase is 97.361(43) Å^3 at 4.2 V, while the initial value of the H3 phase is 91.915(15) Å^3, corresponding to a relative difference in volume of 5.4%, compared to 4.1% and 3.4% for the 1 mol% W samples prepared at 700 °C and 800 °C, respectively. This significant reduction in volumetric deformation during cycling is likely to contribute to the improved cycle life observed in the electrochemical data presented earlier. Similar findings have also been demonstrated in long-term studies of various cathode materials.[93]

Conclusions

The synthesis of W-doped $LiNiO_2$ from commercial hydroxide precursor materials *via* the introduction of ammonium tungstate flux has been investigated. The implications of the flux for the surface morphology and composition were revealed using electron microscopy. At lower temperatures, the tungsten was found to inhibit primary particle growth, and an elongated, grain-like morphology was observed. However, at higher temperatures a more uniform morphology of monolithic grains was observed. Synchrotron XRD and Rietveld analysis suggest the substitution of Ni^{3+} by W^{6+} into the 3a site of the $LiNiO_2$ structure, compensated for charge balance by extra Ni^{2+} in the Li site. The distribution of W doping among primary particles also appears to have a concentration gradient, evidenced by the different primary particle shapes between the interior and the surface of secondary particles. W surface enrichment at grain boundaries has also been observed in samples calcined at higher temperatures. Variable temperature XRD confirms that the inclusion of W can improve the stability of the material at high temperatures during synthesis, with the rate of decomposition found to be reduced compared to the reference sample. Hence, W enables the use of high synthesis temperatures and the preparation of materials with larger primary particles size while avoiding significant structural decomposition. Larger primary grains were observed both at the surface and at the interior of the particles using cross-sectional TEM imaging for samples prepared at higher temperatures. The combined effects of modified morphology and the introduction of W into the structure were found to influence the electrochemical behaviour of the materials, with doped samples exhibiting improved long-term capacity retention, and also improved absolute specific capacity compared to the reference sample after just 10 cycles, for samples prepared between 700 °C and 800 °C. *Operando* XRD collected during cycling of the W-doped materials shows that the introduction of W into the structure does not adversely affect the structural evolution compared to the pristine sample, and the W-doped samples exhibit a smaller difference in unit cell volume between the H2 and H3 phases, which contributes to the improved cycle life. The inclusion of ammonium tungstate in the precursor mixture *via* a simple route, without added processing steps, influences both the surface morphology and structure of the cathode material and delivers benefits to structural stability and electrochemical behaviour. It is therefore an extremely promising and scalable avenue to improve $LiNiO_2$ and high-Ni cathode materials.

Conflicts of interest

The authors declare no competing financial interest.

Acknowledgements

This study was supported by BASF SE. The authors acknowledge MSPD and the ALBA synchrotron for the beamtime awarded under proposal 2020024222. The authors also thank Dr Thomas Bergfeldt (Institute for Applied Materials, KIT) for assistance with ICP-OES measurements, and Dr Holger Geßwein (Institute for Applied Materials, KIT) for assistance with the variable temperature XRD experiments. This work was partly carried out with the support of the Karlsruhe Nano Micro Facility (KNMF, www.knmf.kit.edu), a Helmholtz-Research Infrastructure at Karlsruhe Institute of Technology.

References

1 A. Poullikkas, *Renewable Sustainable Energy Rev.*, 2013, **27**, 778–788.
2 C. P. Grey and D. S. Hall, *Nat. Commun.*, 2020, **11**, 6279.

3 G. Zubi, R. Dufo-Lopez, M. Carvalho and G. Pasaoglu, *Renewable Sustainable Energy Rev.*, 2018, **89**, 292–308.
4 N. Nitta, F. X. Wu, J. T. Lee and G. Yushin, *Mater. Today*, 2015, **18**, 252–264.
5 L. de Biasi, A. O. Kondrakov, H. Geßwein, T. Brezesinski, P. Hartmann and J. Janek, *J. Phys. Chem. C*, 2017, **121**, 26163–26171.
6 M. Wentker, M. Greenwood and J. Leker, *Energies*, 2019, **12**(3), 504.
7 C. Julien, A. Mauger, K. Zaghib and H. Groult, *Materials*, 2016, **9**(7), 595.
8 M. Weiss, R. Ruess, J. Kasnatscheew, Y. Levartovsky, N. R. Levy, P. Minnmann, L. Stolz, T. Waldmann, M. Wohlfahrt-Mehrens, D. Aurbach, M. Winter, Y. Ein-Eli and J. Janek, *Adv. Energy Mater.*, 2021, **11**, 2101126.
9 A. Manthiram, *Nat. Commun.*, 2020, **11**, 1550.
10 M. Li and J. Lu, *Science*, 2020, **367**, 979–980.
11 H. Li, M. Cormier, N. Zhang, J. Inglis, J. Li and J. R. Dahn, *J. Electrochem. Soc.*, 2019, **166**, A429–A439.
12 A. Hebert and E. McCalla, *Mater. Adv.*, 2021, **2**, 3474–3518.
13 J. U. Choi, N. Voronina, Y. K. Sun and S. T. Myung, *Adv. Energy Mater.*, 2020, **10**(42), 2002027.
14 Q. Q. Tao, L. G. Wang, C. H. Shi, J. Li, G. Chen, Z. Xue, J. C. Wang, S. Wang and H. L. Jin, *Mater. Chem. Front.*, 2021, **5**, 2607–2622.
15 D. Goonetilleke, N. Sharma, W. K. Pang, V. K. Peterson, R. Petibon, J. Li and J. R. Dahn, *Chem. Mater.*, 2018, **31**, 376–386.
16 J. R. Dahn, U. Vonsacken and C. A. Michal, *Solid State Ionics*, 1990, **44**, 87–97.
17 G. Dutta, A. Manthiram, J. B. Goodenough and J. C. Grenier, *J. Solid State Chem.*, 1992, **96**, 123–131.
18 P. Bruce, A. Lisowska-Oleksiak, M. Saidi and C. Vincent, *Solid State Ionics*, 1992, **57**, 353–358.
19 M. Bianchini, M. Roca Ayats, P. Hartmann, T. Brezesinski and J. Janek, *Angew. Chem., Int. Ed.*, 2019, **58**, 10434–10458.
20 Q. Xie, Z. Cui and A. Manthiram, *Adv. Mater.*, 2021, **33**, e2100804.
21 Y. Ma, J. H. Teo, D. Kitsche, T. Diemant, F. Strauss, Y. J. Ma, D. Goonetilleke, J. Janek, M. Bianchini and T. Brezesinski, *ACS Energy Lett.*, 2021, **6**, 3020–3028.
22 S. Zhang, J. Ma, Z. L. Hu, G. L. Cui and L. Q. Chen, *Chem. Mater.*, 2019, **31**, 6033–6065.
23 H. H. Sun, H. H. Ryu, U. H. Kim, J. A. Weeks, A. Heller, Y. K. Sun and C. B. Mullins, *ACS Energy Lett.*, 2020, **5**, 1136–1146.
24 D. Weber, D. Tripkovic, K. Kretschmer, M. Bianchini and T. Brezesinski, *Eur. J. Inorg. Chem.*, 2020, **33**, 3117–3130.
25 C. Li, H. P. Zhang, L. J. Fu, H. Liu, Y. P. Wu, E. Ram, R. Holze and H. Q. Wu, *Electrochim. Acta*, 2006, **51**, 3872–3883.
26 C. L. Xu, W. Yang, W. Xiang, Z. G. Wu, Y. Song, G. K. Wang, Y. X. Liu, H. Yan, B. Zhang, B. H. Zhong and X. D. Guo, *Ind. Eng. Chem. Res.*, 2020, **59**, 22549–22558.
27 M. H. Lee, Y. J. Kang, S. T. Myung and Y. K. Sun, *Electrochim. Acta*, 2004, **50**, 939–948.
28 R. Ruess, S. Schweidler, H. Hemmelmann, G. Conforto, A. Bielefeld, D. A. Weber, J. Sann, M. T. Elm and J. Janek, *J. Electrochem. Soc.*, 2020, **167**, 100532.
29 Z. M. Ren, X. H. Zhang, M. Liu, J. J. Zhou, S. Sun, H. Y. He and D. Y. Wang, *J. Power Sources*, 2019, **416**, 104–110.
30 X. Cheng, M. Liu, J. Yin, C. Ma, Y. Dai, D. Wang, S. Mi, W. Qiang, B. Huang and Y. Chen, *Small*, 2020, **16**, e1906433.
31 G. N. Qian, Y. T. Zhang, L. S. Li, R. X. Zhang, J. M. Xu, Z. J. Cheng, S. J. Xie, H. Wang, Q. L. Rao, Y. S. He, Y. B. Shen, L. W. Chen, M. Tang and Z. F. Ma, *Energy Storage Materials*, 2020, **27**, 140–149.
32 H. Y. Li, J. Li, X. W. Ma and J. R. Dahn, *J. Electrochem. Soc.*, 2018, **165**, A1038–A1045.
33 W. Yan, X. Jia, S. Yang, Y. Huang, Y. Yang and G. Yuan, *J. Electrochem. Soc.*, 2020, **167**(12), 120514.
34 H. Ronduda, M. Zybert, A. Szczesna-Chrzan, T. Trzeciak, A. Ostrowski, D. Szymanski, W. Wieczorek, W. Raróg-Pilecka and M. Marcinek, *Nanomaterials*, 2020, **10**(10), 2018.
35 H. Y. Li, J. Li, N. Zaker, N. Zhang, G. A. Botton and J. R. Dahn, *J. Electrochem. Soc.*, 2019, **166**, A1956–A1963.
36 A. Liu, N. Zhang, J. E. Stark, P. Arab, H. Li and J. R. Dahn, *J. Electrochem. Soc.*, 2021, **168**, 040531.
37 A. Liu, N. Zhang, J. E. Stark, P. Arab, H. Li and J. R. Dahn, *J. Electrochem. Soc.*, 2021, **168**, 050506.
38 S. Klein, P. Barmann, O. Fromm, K. Borzutzki, J. Reiter, Q. Fan, M. Winter, T. Placke and J. Kasnatscheew, *J. Mater. Chem. A*, 2021, **9**, 7546–7555.
39 Z. H. Lu, X. J. Huang, H. Huang, L. Q. Chen and J. Schoonman, *Solid State Ionics*, 1999, **120**, 103–107.
40 M. Bianchini, F. Fauth, P. Hartmann, T. Brezesinski and J. Janek, *J. Mater. Chem. A*, 2020, **8**, 1808–1820.
41 D. E. Bugaris and H. C. zur Loye, *Angew. Chem., Int. Ed.*, 2012, **51**, 3780–3811.
42 T. Kimura, *Advances in Ceramics-Synthesis and Characterization, Processing and Specific Applications*, 2011, pp. 75–100.
43 Y. Kim, *ACS Appl. Mater. Interfaces*, 2012, **4**, 2329–2333.
44 S. H. Lee, S. J. Sim, B. S. Jin and H. S. Kim, *Mater. Lett.*, 2020, **270**, 127615.
45 T. Kimijima, N. Zettsu, K. Yubuta, K. Hirata, K. Kami and K. Teshima, *J. Mater. Chem. A*, 2016, **4**, 7289–7296.
46 N. Zettsu, K. Nishikawa, K. Yubuta, K. Sakurai, Y. Yamamoto, Y. Mizuno, S. Oishi and K. Teshima, *J. Mater. Chem. A*, 2015, **3**, 17016–17021.
47 J. Boltersdorf, N. King and P. A. Maggard, *CrystEngComm*, 2015, **17**, 2225–2241.
48 R. Fantin, E. Trevisanello, R. Ruess, A. Pokle, G. Conforto, F. H. Richter, K. Volz and J. Janek, *Chem. Mater.*, 2021, **33**, 2624–2634.
49 X. H. Xiong, Z. X. Wang, P. Yue, H. J. Guo, F. X. Wu, J. X. Wang and X. H. Li, *J. Power Sources*, 2013, **222**, 318–325.
50 D. Pritzl, T. Teufl, A. T. S. Freiberg, B. Strehle, J. Sicklinger, H. Sommer, P. Hartmann and H. A. Gasteiger, *J. Electrochem. Soc.*, 2019, **166**, A4056–A4066.
51 U. H. Kim, D. W. Jun, K. J. Park, Q. Zhang, P. Kaghazchi, D. Aurbach, D. T. Major, G. Goobes, M. Dixit, N. Leifer,

C. M. Wang, P. Yan, D. Ahn, K. H. Kim, C. S. Yoon and Y. K. Sun, *Energy Environ. Sci.*, 2018, **11**, 1271–1279.
52 H. H. Ryu, G. T. Park, C. S. Yoon and Y. K. Sun, *J. Mater. Chem. A*, 2019, **7**, 18580–18588.
53 U.-H. Kim, N.-Y. Park, G.-T. Park, H. Kim, C. S. Yoon and Y.-K. Sun, *Energy Storage Materials*, 2020, **33**, 399–407.
54 K. Zhou, Q. Xie, B. H. Li and A. Manthiram, *Energy Storage Materials*, 2021, **34**, 229–240.
55 M. Yoon, Y. Dong, J. Hwang, J. Sung, H. Cha, K. Ahn, Y. Huang, S. J. Kang, J. Li and J. Cho, *Nat. Energy*, 2021, **6**, 362–371.
56 K. Park, D. J. Ham, S. Y. Park, J. Jang, D. H. Yeon, S. Moon and S. J. Ahn, *RSC Adv.*, 2020, **10**, 26756–26764.
57 W. M. Seong and A. Manthiram, *ACS Appl. Mater. Interfaces*, 2020, **12**, 43653–43664.
58 H. S. Cao, F. H. Du, J. Adkins, Q. Zhou, H. Dai, P. P. Sun, D. Hu and J. W. Zheng, *Ceram. Int.*, 2020, **46**, 20050–20060.
59 H. Li, P. Zhou, F. Liu, H. Li, F. Cheng and J. Chen, *Chem. Sci.*, 2019, **10**, 1374–1379.
60 M. M. E. Cormier, N. Zhang, A. Liu, H. Li, J. Inglis and J. R. Dahn, *J. Electrochem. Soc.*, 2019, **166**, A2826–A2833.
61 I. H. Kwon, H. R. Park and Y. Y. Song, *Russ. J. Electrochem.*, 2013, **49**, 221–227.
62 D. Kitsche, S. Schweidler, A. Mazilkin, H. Geßwein, F. Fauth, E. Suard, P. Hartmann, T. Brezesinski, J. Janek and M. Bianchini, *Mater. Adv.*, 2020, **1**, 639–647.
63 D. Hunyadi, I. Sajó and I. M. Szilágyi, *J. Therm. Anal. Calorim.*, 2013, **116**, 329–337.
64 M. D. Abràmoff, P. J. Magalhães and S. J. Ram, *Biophotonics International*, 2004, **11**, 36–42.
65 F. Fauth, I. Peral, C. Popescu and M. Knapp, *Powder Diffr.*, 2013, **28**, S360–S370.
66 B. H. Toby and R. B. Von Dreele, *J. Appl. Crystallogr.*, 2013, **46**, 544–549.
67 L. Yin, Z. Li, G. S. Mattei, J. Zheng, W. Zhao, F. Omenya, C. Fang, W. Li, J. Li, Q. Xie, E. M. Erickson, J.-G. Zhang, M. S. Whittingham, Y. S. Meng, A. Manthiram and P. G. Khalifah, *Chem. Mater.*, 2019, **32**, 1002–1010.
68 L. De Biasi, G. Lieser, J. Rana, S. Indris, C. Dräger, S. Glatthaar, R. Mönig, H. Ehrenberg, G. Schumacher and J. Binder, *CrystEngComm*, 2015, **17**, 6163–6174.
69 P. J. Chupas, K. W. Chapman, C. Kurtz, J. C. Hanson, P. L. Lee and C. P. Grey, *J. Appl. Crystallogr.*, 2008, **41**, 822–824.
70 G. W. Stinton and J. S. Evans, *J. Appl. Crystallogr.*, 2007, **40**, 87–95.
71 P. Johansson, S. Alvi, P. Ghorbanzade, M. Karlsmo, L. Loaiza, V. Thangavel, K. Westman and F. Aren, *Batteries Supercaps*, 2021, **4**, 1785–1788.
72 G.-T. Park, H.-H. Ryu, N.-Y. Park, C. S. Yoon and Y.-K. Sun, *J. Power Sources*, 2019, **442**, 227242.
73 G. Z. Shang, Y. W. Tang, Y. Q. Lai, J. Wu, X. Yang, H. X. Li, C. Peng, J. F. Zheng and Z. A. Zhang, *J. Power Sources*, 2019, **423**, 246–254.
74 W. Li, J. Zhang, Y. Zhou, W. Huang, X. Liu, Z. Li, M. Gao, Z. Chang, N. Li, J. Wang, S. Lu, X. Li, W. Wen, D. Zhu, Y. Lu and W. Zhuang, *ACS Appl. Mater. Interfaces*, 2020, **12**, 47513–47525.
75 Y. Kim, H. Park, J. H. Warner and A. Manthiram, *ACS Energy Lett.*, 2021, **6**, 941–948.
76 C. T. Chantler, K. J. Olsen, R. A. Dragoset, A. R. Kishore, S. A. Kotochigova and D. S. Zucker, *X-Ray Form Factor, Attenuation and Scattering Tables (version 2.0)*, 2003, http://physics.nist.gov/ffast.
77 R. D. Shannon, *Acta Crystallogr., Sect. A: Cryst. Phys., Diffr., Theor. Gen. Crystallogr.*, 1976, **32**, 751–767.
78 C. Liang, F. Kong, R. C. Longo, C. Zhang, Y. Nie, Y. Zheng and K. Cho, *J. Mater. Chem. A*, 2017, **5**, 25303–25313.
79 L. Yin, G. S. Mattei, Z. Li, J. Zheng, W. Zhao, F. Omenya, C. Fang, W. Li, J. Li, Q. Xie, J. G. Zhang, M. S. Whittingham, Y. S. Meng, A. Manthiram and P. G. Khalifah, *Rev. Sci. Instrum.*, 2018, **89**, 093002.
80 H. H. Sun, U. H. Kim, J. H. Park, S. W. Park, D. H. Seo, A. Heller, C. B. Mullins, C. S. Yoon and Y. K. Sun, *Nat. Commun.*, 2021, **12**, 6552.
81 Y.-Q. Sun, W. Fu, Y.-X. Hu, J. Vaughan and L.-Z. Wang, *Tungsten*, 2021, **3**, 245–259.
82 A. Hirano, R. Kanno, Y. Kawamoto, Y. Takeda, K. Yamaura, M. Takano, K. Ohyama, M. Ohashi and Y. Yamaguchi, *Solid State Ionics*, 1995, **78**, 123–131.
83 E. McCalla, G. H. Carey and J. R. Dahn, *Solid State Ionics*, 2012, **219**, 11–19.
84 C. H. Shen, Q. Wang, F. Fu, L. Huang, Z. Lin, S. Y. Shen, H. Su, X. M. Zheng, B. B. Xu, J. T. Li and S. G. Sun, *ACS Appl. Mater. Interfaces*, 2014, **6**, 5516–5524.
85 H. Y. Li, N. Zhang, J. Li and J. R. Dahn, *J. Electrochem. Soc.*, 2018, **165**, A2985–A2993.
86 M. Y. Song, S. Kwon, I. Kwon and H. Park, *J. Appl. Electrochem.*, 2007, **37**, 421–427.
87 T. Ohzuku and Y. Makimura, *Res. Chem. Intermed.*, 2006, **32**, 507–521.
88 M. Mock, M. Bianchini, F. Fauth, K. Albe and S. Sicolo, *J. Mater. Chem. A*, 2021, **9**, 14928–14940.
89 P. Kurzhals, F. Riewald, M. Bianchini, H. Sommer, H. A. Gasteiger and J. Janek, *J. Electrochem. Soc.*, 2021, **168**(11), 110518.
90 L. de Biasi, A. Schiele, M. Roca-Ayats, G. Garcia, T. Brezesinski, P. Hartmann and J. Janek, *ChemSusChem*, 2019, **12**, 2240–2250.
91 M. Duffiet, M. Blangero, P. E. Cabelguen, C. Delmas and D. Carlier, *J. Phys. Chem. Lett.*, 2018, **9**, 5334–5338.
92 K. Mukai, Y. Kishida, H. Nozaki and K. Dohmae, *Chem. Mater.*, 2013, **25**, 2828–2837.
93 S. Schweidler, L. de Biasi, G. Garcia, A. Mazilkin, P. Hartmann, T. Brezesinski and J. Janek, *ACS Appl. Energy Mater.*, 2019, **2**, 7375–7384.